Role of temperature in the development of micro-scale damage in CFRP laminates through interrupted high-rate loading and synchrotron phase-contrast μ-CT

Xiyao Sun[a], Bratislav Lukić[b,c], Kai Liu[a], David Sory[a], Maria Lissner[a], Justus Hoffmann[a], David Chapman[a], Nik Petrinic[a] and Daniel Eakins[a,*]

[a]Department of Engineering Science, University of Oxford, Parks Road, Oxford, OX1 3PJ, UK
[b]European Synchrotron Radiation Facility, 71 Av. des Martyrs, Grenoble, 38000, France
[c]Henry Royce Institute for Advanced Materials, Department of Materials, The University of Manchester, Manchester, M13 9PL, UK

ARTICLE INFO

Keywords:
CFRP composites
Impact behaviour
Synchrotron X-ray tomography
Temperature-dependent damage

ABSTRACT

Understanding the evolution of damage in aerospace-grade CFRP composites after high-speed impact events is crucial for the safe design of components that can withstand dynamic loads. In this study, the temperature-dependent mechanisms of micro-scale damage in angle-ply CFRP were studied through a combination of interrupted high-rate compression experiments and synchrotron X-ray phase-contrast micro-tomography employing deep-learning-aided image analysis. Despite the earlier damage onset at low temperatures, all specimens tested have similar apparent-yield strains. The mechanisms responsible for the early damage, namely mode-II-dominant fracture in surface and subsurface plies, are observed to be similar at both low and room temperature, with the surface ply cracks the first to develop into opened damage. After the occurrence of the middle-ply opened damage, while the room-temperature specimens dissipate energy through deformation and cracking originating from the specimen loading ends, glassy inter-ply fractures propagating from the surface towards the middle plies are the root of the rapid drop in specimen strength at low temperatures after the apparent-yield point.

1. Introduction

Carbon-fibre reinforced polymer (CFRP) composites are increasingly used in a variety of high-performance engineering applications, including aircraft, automotive, ships and satellites owing to their merits such as excellent specific strength and corrosion resistance [1–3]. However, their impact resistance is particularly important in these applications due to the inherent risk of high-speed foreign object impact during service. Off-fibre-axis compressive load resistance is normally a weakness of CFRP laminates and therefore a crucial factor that limits application [4]. As a result, understanding the nascence of damage mechanisms under high strain-rate (HSR) compression is imperative to improve the numerical simulation and design of CFRP.

While methods exist for *in-situ* investigation of subsurface damage in CFRP under quasi-static loading [5–7], experimentally capturing and characterising the damage initiation of CFRP laminates under HSR loading has been challenging because the process is normally transient. It is difficult to interrupt and resume during the loading, which gives rise to challenges in observing the internal microstructural damage mechanisms. *In-situ* surface damage observation suggests that fibre kinking is the dominant failure mechanism for unidirectional (UD) laminates under in-plane loading [8]. Cross-ply (CP) laminates normally have slightly more complex damage as a combination of fibre kinking, ply delamination and matrix cracking owing to the introduction of 90° fibres [4, 9]. Nano-scale *in-situ* crack observation performed by using synchrotron radiation X-ray computed tomography (CT) reveals that cracks in tested CFRP specimens initiated at the fibre/fibre contacting face in resin-thin regions and at fibre/resin interfaces in the resin-rich regions under opening loads [10]. Wang et al.[11] observed the formation of local fibre tilting prior to the formation of micro-scale kink-band in glass-fibre reinforced polymer (GFRP) with a similar *in-situ* X-ray CT approach. Final failure modes of CP [12], angle-ply (AP) [13], quasi-isotropic (QI) [14] and biaxial braided (BB) [15] laminates were investigated and found to be mainly inter-ply delamination under HSR in-plane compression.

The susceptibility of composites' mechanical properties to their ambient temperatures has been well established in previous research [16–20]. However, few existing studies have examined the associated micro-mechanisms of internal damage. Post-mortem inspection conducted by Sanchez-Saez et al. [21] and Ou et al. [22] indicate that both low and high temperatures can diminish the bonding strength at fibre/matrix interfaces and lead to a higher degree of fibre debonding and ply delamination. Furthermore, under tension, three-point bending and ballistic penetration, damage in CFRP laminates can develop more quickly and extensively through the bulk, with severe ply delamination taking place at lower temperatures [23–25].

*Corresponding author
xiyao.sun@eng.ox.ac.uk (X. Sun); daniel.eakins@eng.ox.ac.uk (D. Eakins)
shock.eng.ox.ac.uk (D. Eakins)
ORCID(s): 0009-0005-2383-5750 (X. Sun); 0000-0002-3535-5624 (D. Eakins)

Label	Volume, mm^3	Weight, g	Designed final strain, %
Room: 23 ± 2, °C			
IF1	24.85	38.20	No interrupt
IF2	26.37	40.16	No interrupt
IF3	25.92	40.06	No interrupt
RM1	25.46	39.23	2.33
RM2	24.93	38.02	2.99
RM3	26.18	40.23	3.99
RM4	25.56	39.17	8.00
RM5	25.83	39.53	13.00
Cold: −50 ± 2, °C			
IF4	25.91	39.45	No interrupt
IF5	24.42	37.64	No interrupt
IF6	23.52	36.62	No interrupt
CL1	24.85	38.48	2.33
CL2	24.56	38.11	2.66
CL3	26.10	40.02	3.32
CL4	25.73	39.39	4.32
CL5	24.94	38.23	8.31

Table 1
Specimen details and testing conditions. All specimens were dynamically compressed along the plane of the laminates at an approximate strain-rate of 2500 s^{-1}.

Characterising the temperature effects on the damage of anisotropic composites such as CFRP laminates upon impact is an enduring challenge, which hinders the understanding of damage mechanisms and the development of damage prediction in composite engineering applications. Although the previous work [26] revealed the HSR damage evolution of CFRP laminates at different temperatures via *in-situ* dynamic X-ray imaging, only limited information was retrieved at the damage onset stage, especially through the laminate thickness. Other recent research using dynamic X-rays [27–30] suffers from similar problems owing to the low-resolution and 2D projection nature of this technology. In this context, the present research aims to investigate micro-structural damage initiation and propagation in AP CFRP laminates under HSR in-plane compression. Impact loading was precisely interrupted at specific specimen strains at varying *in-situ* testing temperatures to control the extent of damage. High-resolution synchrotron phase-contrast CT was utilised to observe the micro-scale damage at different loading stages. Finally, the micro-structural damage morphology and mechanisms of the tested specimens at different temperatures and loading stages were characterised, analysed and compared.

2. Materials and Methods

2.1. Material and specimen

The tested carbon-fibre reinforced polymer (CFRP) laminate is composed of a high-performance epoxy resin provided by Hexcel Corporation and "standard modulus" carbon fibres provided by Toray Industries, Inc. The laminates were autoclave-cured using the following process: heating to 180 °C at a rate of 1-2°C min^{-1}, dwelling for 120 mins, and cooling back to room temperature at a rate of 2-5 °C min^{-1}. A hand lay-up method using UD fibre prepregs was introduced to produce a $[+45/-45]_{4s}$ AP lamination with a nominal thickness of 3 mm. The CFRP specimens were cut into small cubes ($3\times3\times3$ mm^3) to fit the field of view of the high-resolution X-ray micro-computed tomography (μ-CT). It should be noted that the small specimen size necessary for the current experimental approach might lead to the specimen response not being fully representative of the bulk or structural scale. However, the focus of the present research is to investigate the temperature effect on CFRP micro-scale damage mechanisms involving the behaviours of fibres, matrix, and their interactions under high-rate loading.

As listed in Table 1, 16 specimens in total were tested at room (23 °C) and cold temperature (−50 °C). Among them, 6 specimens (IF1 - 6) were impacted without specimen strain interruption to evaluate the overall stress-strain behaviours of the tested CFRP laminates. Based on this, 5 representative strain levels were selected as the target strain for each temperature. The loading of the remaining 10 specimens (RM1 - 5 and CL1 - 5) was interrupted at the target strains to evaluate the specimens' damage at the different loading stages.

2.2. High strain-rate loading

A split-Hopkinson pressure bar (SHPB) system was used to apply HSR in-plane loading to the CFRP specimens. The system is composed of a 200 mm striker bar, a 1300 mm input bar and a 1100 mm output bar. All the bars are made of titanium alloy (Ti-6Al-4V) with a diameter of half an inch (∼12.7 mm). Two 3 mm-thick Ti-6Al-4V loading platens with the same diameter were placed between the specimens and bars to avoid the bars being damaged. A momentum trap system was installed on the input bar to prevent the secondary impact of the specimens.

Strain control collars with different spacer thicknesses were manufactured from Ti-6Al-4V titanium alloy, and were mounted at the end of the output bar, as illustrated in Fig. 2. The specimen is sandwiched between the input and output bars in the open area beside the collar spacer. Upon loading, the input bar will first compress the specimen. Once the specimen is compressed to the same thickness as the collar spacer, the input bar will come in contact with the collar spacer and create a 'hard stop' to prevent further deformation of the specimen. In this way, the thickness of the spacers was chosen to limit the maximum strain applied to the specimen.

All HSR loading tests were performed with a projectile impact velocity of about 13.8 m s^{-1}, producing an approximate strain-rate of 2500 s^{-1} onto 3 mm length specimens. Prior to the interrupted strain tests, HSR loading tests without strain interruption (impact to failure) were also conducted to evaluate the mechanical behaviours of tested CFRP laminates at room and low temperatures. It is worth mentioning that the mechanical responses of the specimens in this research mainly serve as a reference for the damage analysis. The specimen stress calculation directly adopts the cross-sectional area of the specimens, rather than following

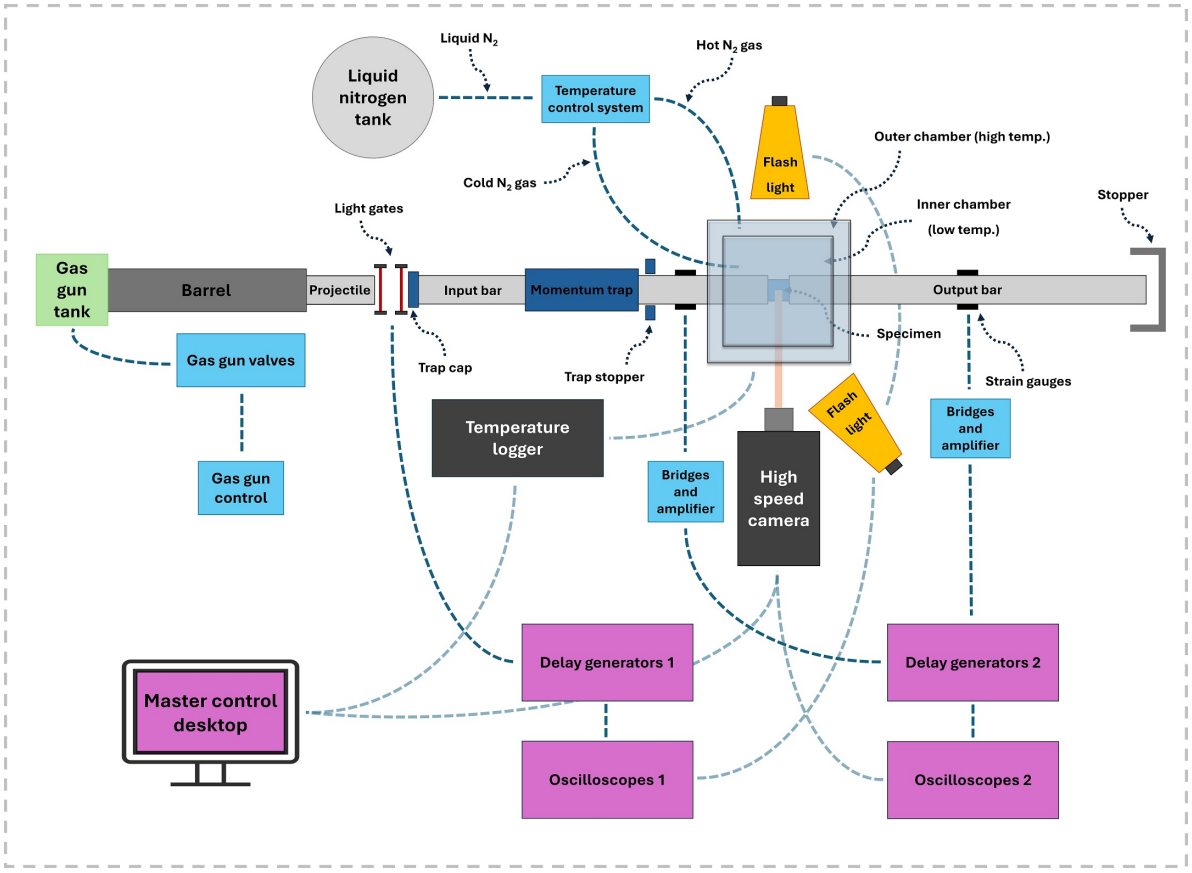


Figure 1: Schematic of the experimental setup depicting the HSR loading apparatus, temperature control, temperature monitoring, strain recording, and imaging systems. Two flashes were set up to compensate for light obstruction caused by the strain control collars. The flash facing the front of the specimen (on the same side as the camera) was to illuminate the speckles for strain tracking; the one opposite the camera was for backlighting to locate the specimen and check for gaps at the specimen/platen interfaces.

ASTM D3518/D3518M [31] for in-plane shear testing of ±45° laminates.

2.3. Test temperature control

A bespoke double-layer PMMA (polymethyl methacrylate) box was designed and manufactured as the cryogenic chamber for the HSR loading tests. During the low-temperature tests, the impact of specimens was taking place in the inner box filled with cold (approx. −80 °C) nitrogen gas. In the meantime, the hot (approx. 50 °C) nitrogen gas was injected into the outer chamber, which prevents frost and mist from forming on the inner window by removing the ambient moisture and on the outer window by maintaining the window temperature above 0 °C. The temperature control of the injection flow was achieved by using a bespoke flow and temperature control system. The system inlet was connected to a liquid nitrogen tank. The injected liquid nitrogen was first converted into gas in a nitrogen reservoir. Then, the cold nitrogen gas was divided into two flows, one flow was heated to the target testing temperature and injected into the inner chamber of the box, and another flow was heated to high temperatures and filled into the outer chamber. Temperature measurement was performed at multiple locations in the inner and outer chamber to ensure a stable temperature and mist control.

2.4. Strain control and measurement

Strain gauges were applied in these tests to monitor the stress-strain behaviours of the specimens. They were mounted 550 mm uprange of the input bar/specimen interface and 500 mm downrange of the output bar/specimen interface. By assuming one-dimensional wave propagation, the engineering stress and strain of the specimens can be estimated based on the measured bar strain and their time difference [32]. In addition, an extra strain monitor measure - a visible-light high-speed camera - was also introduced. Digital image correlation (DIC) was performed on top of the recorded images using `GOM Correlation` to monitor the specimen strain throughout the loading process. The interruption strain measured by DIC was adopted as ε_{interr} (the strain reference) for damage analysis. Apart from that, the theoretical maximum specimen strain was also estimated with the assumptions of linear elastic deformation of collar materials. The peak force, F_{max} acting on the strain control collars and specimens can be obtained using,

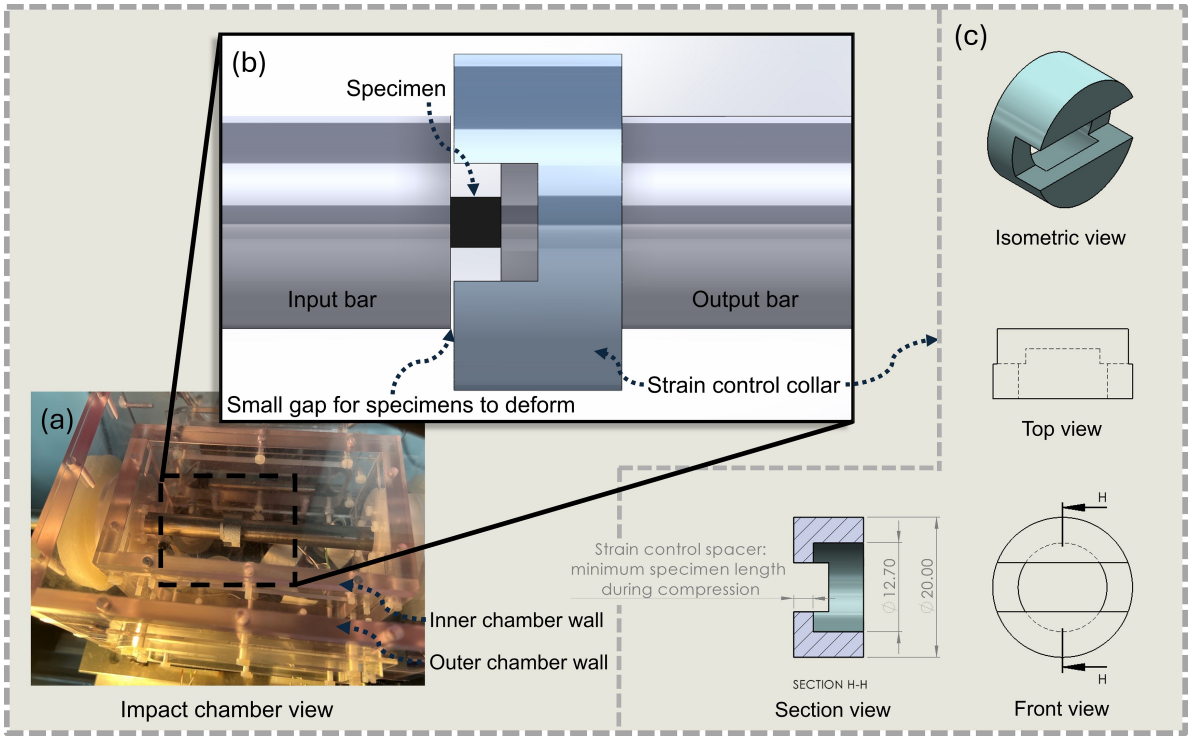


Figure 2: Strain control collar design and setup: (a) photo of the collar mounted on the bars in the impact chamber, (b) zoom-in schematic illustration and (c) detailed drawings. The strain control collars were manufactured with high precision to produce quality specimen strain control. The tolerance of the strain control spacer was maintained within ±10 µm.

$$F_{max} = A_b E_b \varepsilon_{b,max}, \tag{1}$$

where A_b and E_b are the cross-sectional area and the elastic modulus of the output bar. The maximum compressive strain of the output bar is noted as $\varepsilon_{b,max}$. The supporting force provided by the specimen at the point of peak loading force (F_{sp}) can be estimated as,

$$F_{sp} = A_b \sigma_{sp}. \tag{2}$$

The maximum stress of the tested CFRP laminates in the design strain interruption range (σ_{sp}) is around 300 MPa. Therefore, by assuming this value, the approximated collar spacer strain, ε_c can be represented by,

$$\varepsilon_c = \frac{F_{max} - F_{sp}}{A_c E_c}, \tag{3}$$

where A_c is the cross-sectional area of the collars that is in contact with the faces of the bar end, and E_c is the elastic modulus of the collar material. The maximum theoretical strain of the specimens, ε_t will be the summation of specimen strain before and after the collar's intervention, ε_{t1} and ε_{t2}, expressed as,

$$\varepsilon_t = \varepsilon_{t1} + \varepsilon_{t2} = \frac{(l_{sp} - d_c) + \varepsilon_c d_c}{l_{sp}}, \tag{4}$$

where the length of the specimens was noted as l_{sp}, and d_c is the thickness of the collar spacer.

Statistic analysis was carried out to assess the validity of the strain control during impact loading. The standard deviation of the four strain data sets (S_ε), including the designed strain (ε_d), theoretically calculated strain (ε_t), DIC-measured strain (ε_i) and gauge-measured strain (ε_g), can be expressed as,

$$S_\varepsilon = \sqrt{\frac{1}{4}\sum_{n=1}^{4}(\varepsilon_n - \bar{\varepsilon})^2}, \tag{5}$$

where $\bar{\varepsilon}$ stands for the mean of the four strain sets. Finally, the dispersion of the strain data is estimated using the coefficient of variation (CV_ε),

$$CV_\varepsilon = \frac{S_\varepsilon}{\bar{\varepsilon}}. \tag{6}$$

2.5. Micro-computed tomography scanning

As listed in Table 1, all specimens were scanned with µ-CT prior to the impact tests (pre-scan) to study the original state of the laminates' internal structure. Among them, 10 specimens were also scanned after the tests (post-scan) to examine and characterise the damage of specimens at different temperatures. The µ-CT scanning was performed at

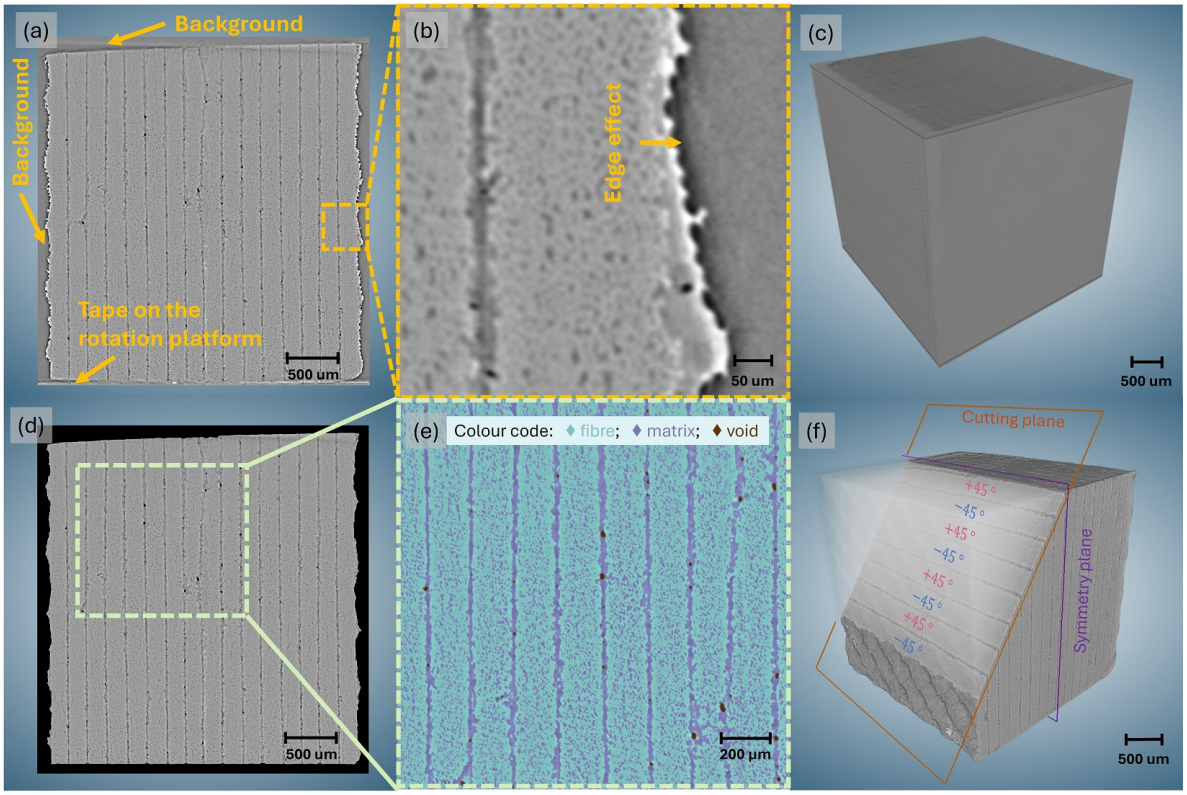


Figure 3: Tomographic reconstruction of an original, uncompressed specimen: (a) original 2D slice, (b) magnified view, and (c) 3D volume rendering without removing the background and rotation platform; (d) 2D slice, (e) magnified view, and (f) 3D volume rendering after removing the background and rotation platform. The background cannot be removed by simple thresholding because its grey values are similar to the specimen's matrix. Additionally, the platform was a similar grey value and texture to the specimen, necessitating removal using a bespoke `Python` script.

a synchrotron X-ray beamline - ID19 at the European Synchrotron Radiation Facility (ESRF), France with a voxel size of 2.1 μm^3. Synchrotron-based X-ray imaging can achieve higher scanning efficiency (i.e., shorter scanning times) and resolution compared to laboratory-based µ-CT by virtue of the high energy flux and microscopic source size [5]. Apart from that, by taking advantage of the brilliance and (partial-)coherence of synchrotron X-ray radiation gain through free-space propagation, the micro-damage inside the specimens can be enhanced via X-ray phase contrast tomography of weakly absorbing specimens [33]. The specimens were illuminated with a filtered white beam emitted by the beamline's wiggler insertion device located 150 m upstream of the specimens. The two sets of in-vacuum slits were used to focus the beam onto the desired field of view (FoV) and for heat moderation coming from off-axis energy spread. A series of filters (i.e., diamond, aluminium and copper) were used, providing impinging wide-spectrum radiation with a peak energy of 40 keV. The indirect detector consisted of a 3× magnification tandem lens (300 mm:100 mm, Hasselblad, Sweeden) coupled to a sCMOS camera (pco.edge 5.5, PCO AG, Germany) and a 250 µm thick LuAG:Ce scintillator. The detector was positioned 250 mm away from the specimens, allowing for sufficient edge enhancement to form through the propagation-based phase contrast effect. During a full rotation of 360 degrees, 6000 projections were taken. The 3D tomographic reconstructions were carried out with ESRF reconstruction software employing a single-distance phase-retrieval approach [34] and the ratio of the real and complex part of the refraction index (δ/β) of 120.

The pre- and post-scans were performed at two separate beamtimes. Hence, image normalisation and registration between pre- and post-scans are necessary to enable qualitative and quantitative comparisons. Image registration was implemented using image computation software - `3D Slicer` [35]. A `Python` code was developed to normalise the pre- and post-scan images. A U-Net-based deep learning model embedded in `Dragonfly 3D World` software [36] was trained and implemented together with `Python` scripts to remove the noise and unwanted background in the obtained µ-CT images. The `MaxEntropy` thresholding method was used to segment the void and damage from the specimens. The qualitative and quantitative damage analyses were then carried out using a workflow involving `ImageJ`, `Dragonfly` and `Python`.

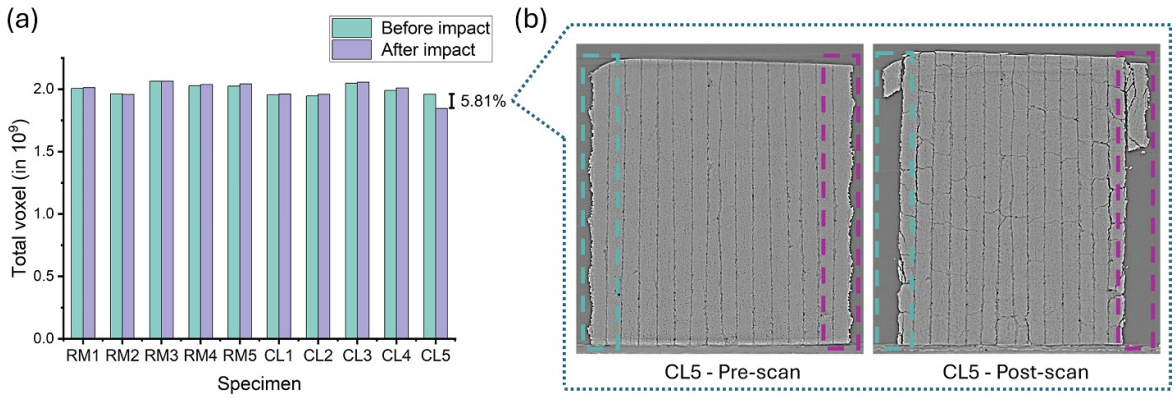


Figure 4: (a) Total number of specimen voxels after removing backgrounds. Good agreement can be found between pre-scans and post-scans for most specimens with less than 1 % differences. (b) A slice comparison between CL5 pre-scan and post-scan before removing the background showing surface plies on both sides fractured and detached from the specimen after the impact.

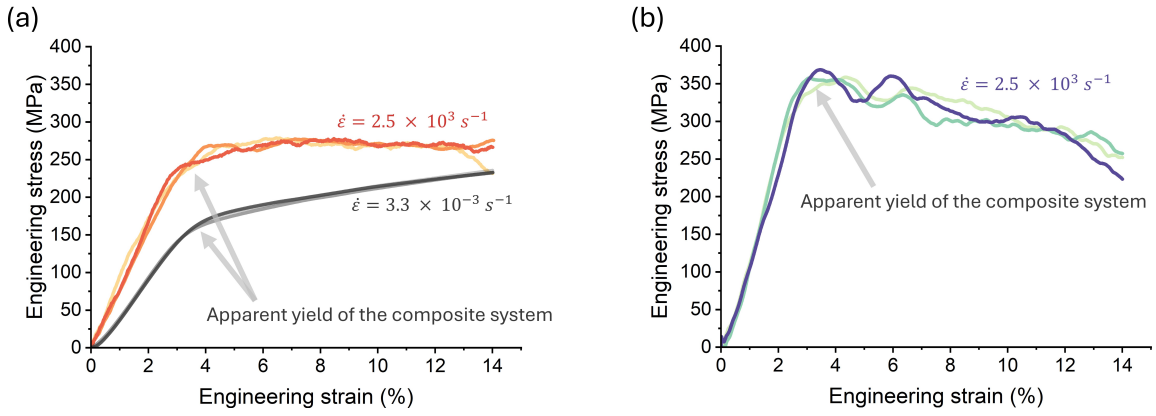


Figure 5: Mechanical responses of the specimens at about 2.5×10^3 s^{-1} strain rate. Stress-strain curves under impact-to-failure loading for (a) room temperature specimens with the quasi-static (3.3×10^{-3} s^{-1}) loading curves as a baseline and (b) low-temperatures specimens. Please note that the quasi-static stress-strain curves were obtained from the load cell and cross head displacement of the universal loading machine. The low-temperature specimens demonstrate evidently higher peak strength, followed by a quicker stress drop. The post-apparent-yielding behaviours of the specimens at three test conditions shift from strain hardening (quasi-static at room temperature) to stress flowing (HSR at room temperature) and then strain softening (HSR at low temperatures). "Apparent-yield", in the present research, refers to the sudden change in gradient of the stress-strain responses of the specimens [37].

3. Results

3.1. Specimen micro-structure

2D and 3D image visualisations are presented in Fig. 3. The background's grey value is similar to that of the specimen's matrix due to the superposition effect of X-ray phase contrast between the background (i.e. air) and specimen. Edge effects are shown along the irregular boundary of the specimens, seen as a dark and light fringe following the specimen outline (Figs. 3a and b). The specimens' internal features cannot be effectively recognised and extracted without removing the background and specimen support from the original scans (Fig. 3c). Thus, a trained deep-learning model was used and demonstrates high accuracy in this complex background recognition and segmentation scenario (Fig. 3d).

A layer of tape used to secure the specimens on the rotation platform shows a similar grey value and texture to the specimens (Fig. 3a). A custom-developed `Python` script can help aid the deep learning model in accurately segmenting the tape on the platform. As shown in Fig. 4, good volume consistency can be found between the pre-scans and post-scans of most specimens, suggesting a reliable background removal method. The discrepancy for CL5 is slightly higher ($\sim$ 5.81 %) because the surface plies detached from the laminates at large strain during the impact.

The processed specimen volume shown in Fig. 3(e and f) demonstrates +45° and −45° unidirectional plies are laid up in turn and symmetry about the middle plane forming a total

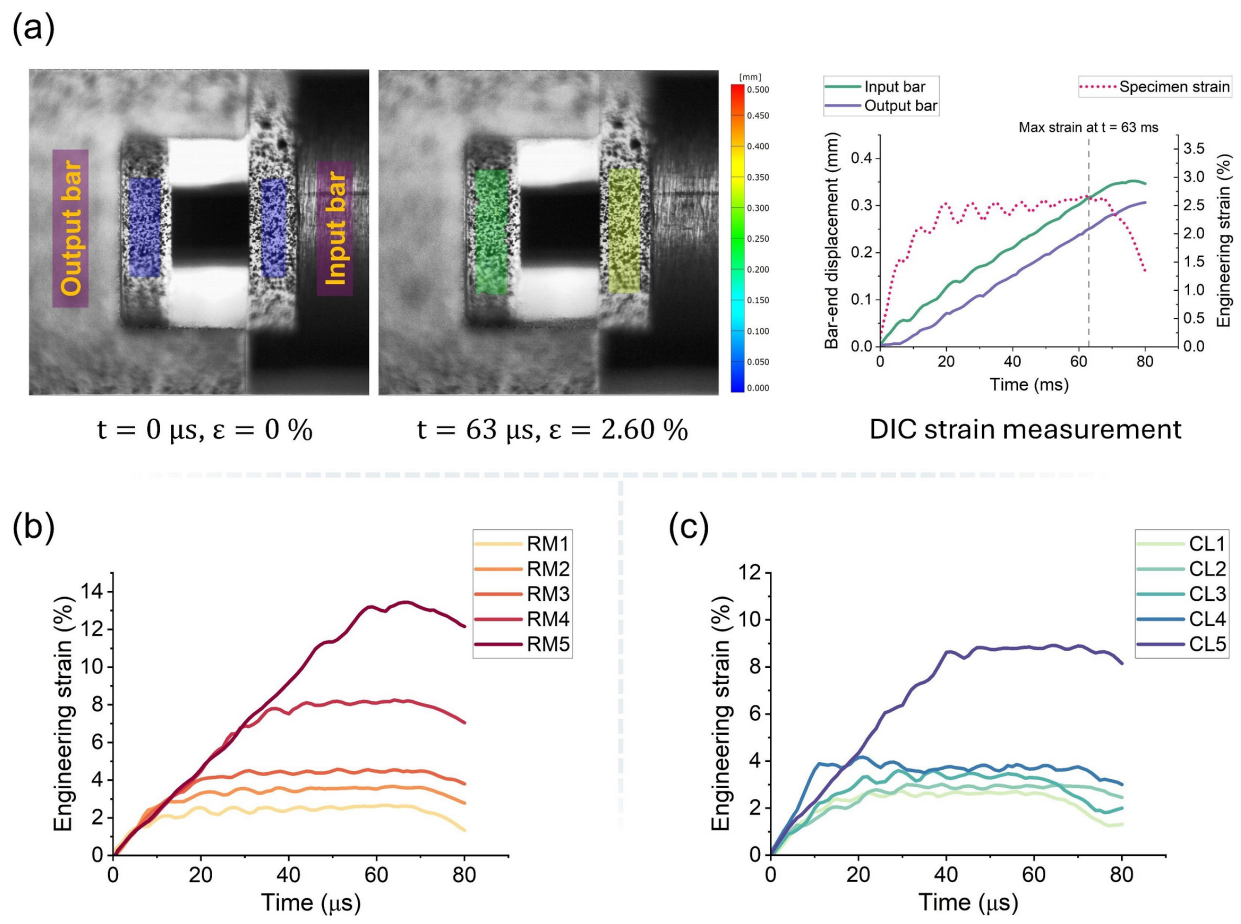


Figure 6: Specimen strain measurement by performing DIC on visible light images captured during impact loading: (a) an example using specimen RM1 demonstrating speckle recognition and displacement tracing; strain measured for specimens at (b) room and (c) low temperatures. The sudden flattening of strain-time curves indicates the intervention of the strain control collars. The specimen strain was interrupted and maintained near the designed strain levels after the input bar end came into contact with the collars.

of 16 plies with each in the approximate thickness of 170 µm. 5 µm-diameter carbon fibres are densely packed in each ply, resulting in an overall measured fibre volume fraction of about 60 % (Fig. 3e). Voids with diameters ranging from 5 to 20 µm can be found in the resin-rich area between plies occupying a slight volume of around 0.2 % in the specimens, similar to the data from the literature [38]. No crack-shaped defects or damage at the micro-scale level and above can be found in all the pre-scanned specimens.

3.2. Mechanical properties

Fig. 5 shows the mechanical response of the HSR load tests without interrupting the specimen strain during the loading (impact to failure). Despite the similar loading rate, the specimens tested at low temperatures exhibit significantly higher peak strength (approximately 35 %) than the room-temperature specimens [26]. For the room-temperature specimens (Fig. 5a), a stable flow stress stage appears after the elastic-like deformation phase, different from an obvious strain-hardening behaviour of the specimen under quasi-static loading ($\sim 10^{-3}s^{-1}$), as shown by the grey curves. In contrast, the low-temperature specimens exhibit distinct stress peaks, followed by noticeable stress drops. Nevertheless, the elastic-like deformation stage for specimens at both temperatures seems to end between 3 to 4 % strain, similar to their quasi-static reference. Thus, the specimens' interruption strain (ε_{interr}), listed in Table 1, was specifically chosen to range from under 3 % to over 4 % strain, ensuring coverage of varying damage levels in the specimens.

3.3. Strain interruption

Fig. 6a demonstrate an example of strain measurement via tracking the movement of the loading platens on both sides of the specimens. The analysed strain development with time obtained from DIC for room- and low-temperature specimens are plotted in Figs. 6b and 6c, respectively. The produced ε_{interr} increases progressively from RM1 to 5 and from CL1 to 5. The specimens experienced a free compression stage without any collar interference, reflected by a linear-like increase at the start of the loading, followed by a bar/collar interaction stage where the curves level out with

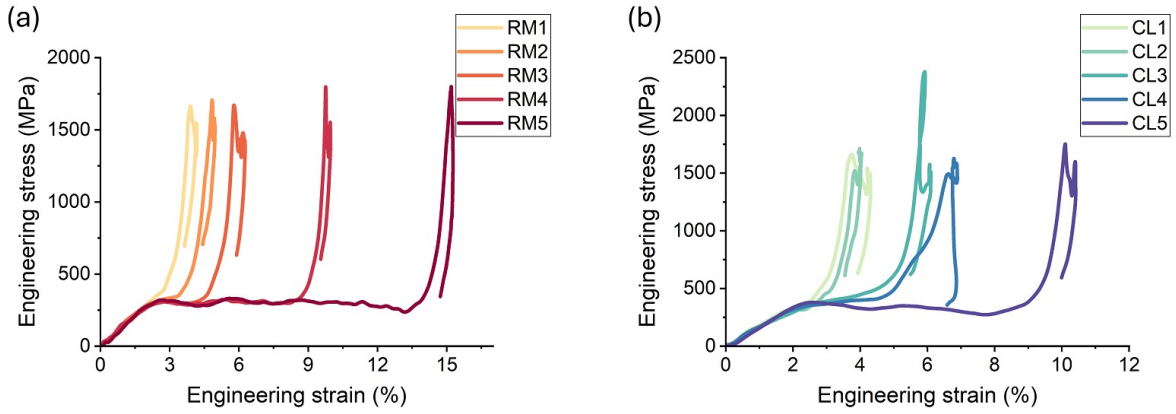


Figure 7: Stress-strain curves of the specimens with strain interruption at (a) room and (b) low temperatures. The starting points of the sudden stress rise indicate the beginning of strain intervention.

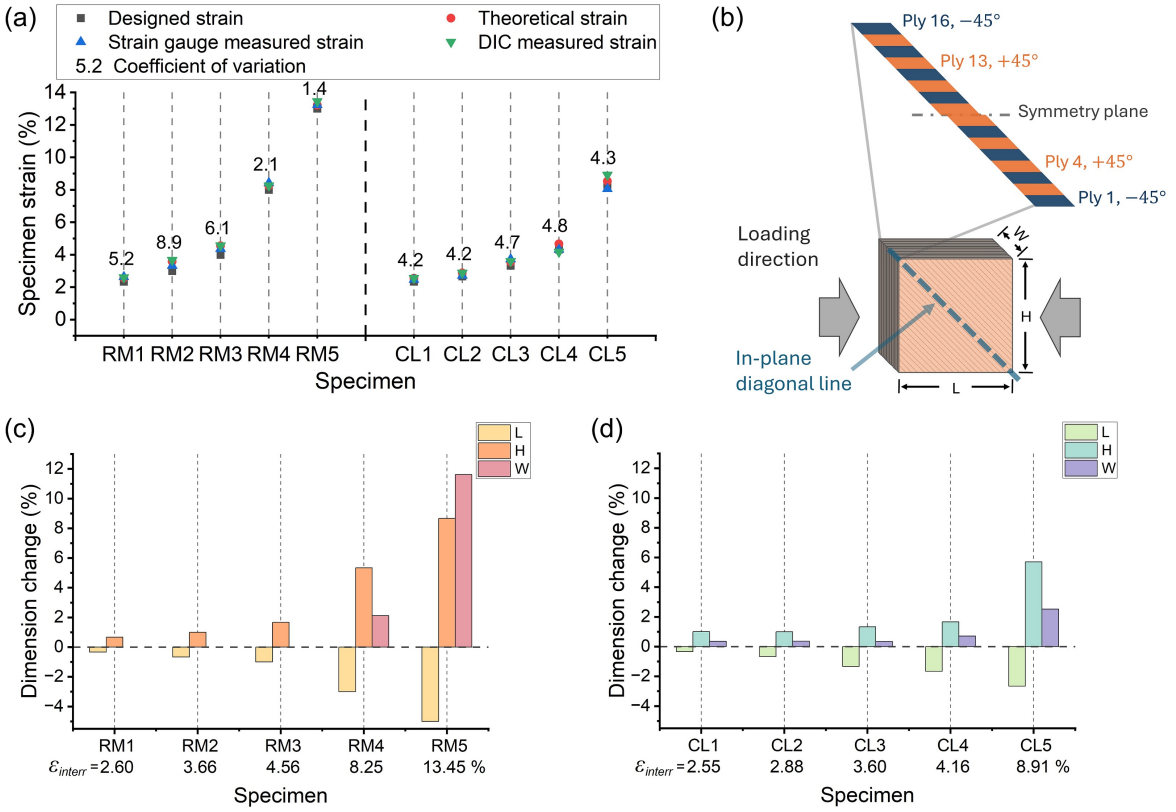


Figure 8: Specimen dimension change after the impact: (a) comparison between designed strain, theoretically estimated strain and measured strain of specimens with the coefficients of variation; (b) specimen geometry, loading and ply configurations; dimension change induced by the impact for (c) room- and (d) low-temperature specimens. As a recap: the designed strain is the target strain from the experiment plan (see Table 1); the theoretical strain is the strain estimation based on the measured force in the bars and the mechanical properties of the specimens and collars (see Section 2.4); the strain-gauge-measured strain was obtained from the SHPB analysis (see Section 2.4); and the DIC-measured strain was determined from the high-speed images (see Section 3.3).

observable strain oscillations. The specimen stress-strain relations extracted from strain gauge signals is presented in Figs. 7a and 7b for room- and low-temperature specimens, respectively. The sudden rises in stress also indicate the points at which the input bar ends came into contact with the strain control collars.

Together with the designed and theoretically calculated strain, in total, four sets of strain (design strain, theoretically calculated strain, DIC-measured strain and gauge-measured strain) are plotted in Fig. 8a. Statistic assessment by calculating the coefficient of variation suggests a minor dispersion (less than 10 %) between the four sets of strain data for

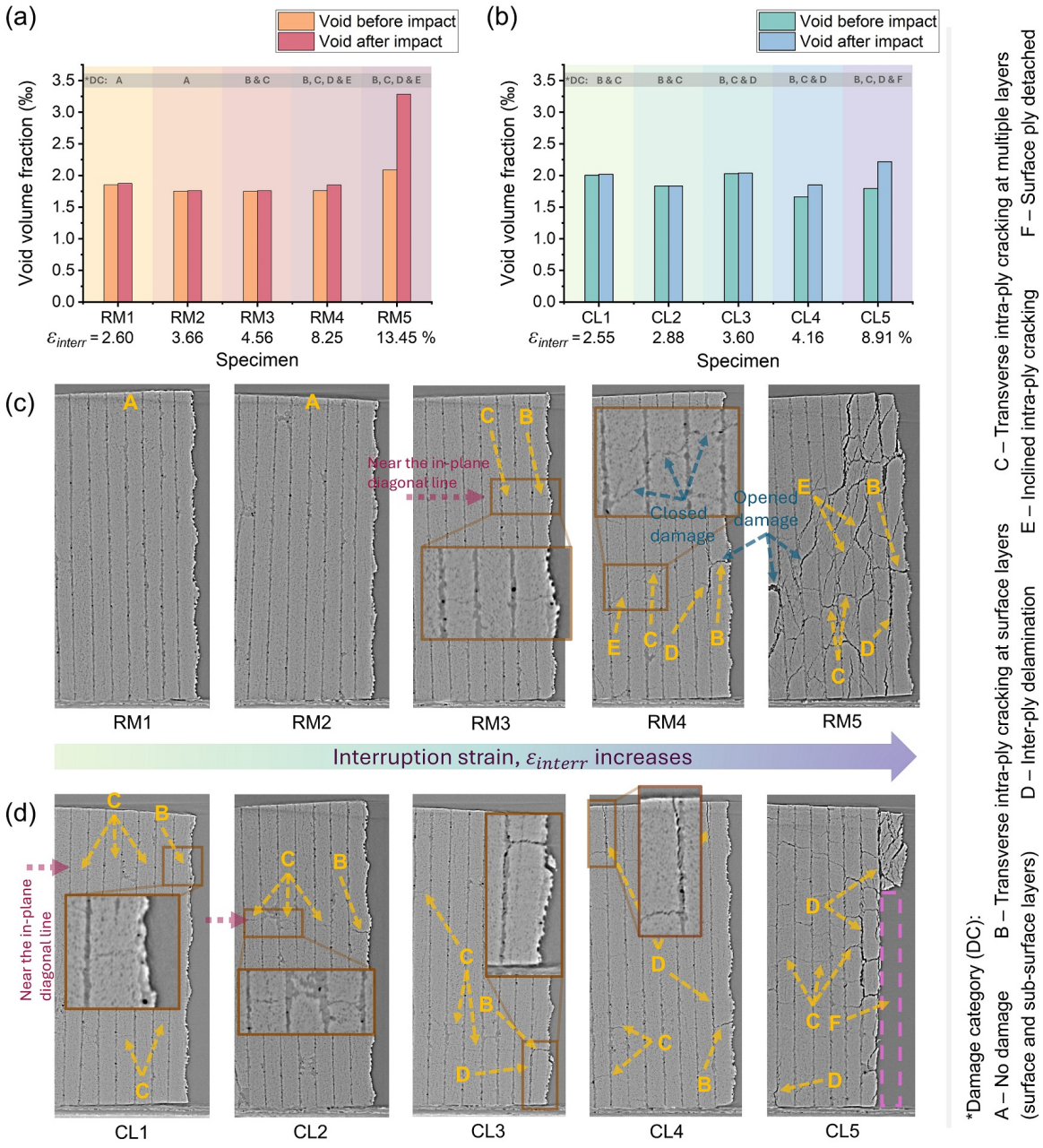


Figure 9: Specimen internal structure change with strain increase. Void volume fractions before and after impact for (a) room- and (b) low-temperature specimens. Good void volume consistency can be found in the specimens with low ε_{interr}. Damage development overview shown in the symmetric half for (c) room- and (d) low-temperature specimens. The damage volume increases and the damage morphology evolves at both temperatures with increasing ε_{interr}.

all specimens. This demonstrates the validity of the strain interruption in this impact experiment.

The nominal dimension change of the specimens after the impact was measured and is visualised in Figs. 8c and 8d. The height (H) and width (W) of all specimens increased with the increasing strain at both temperatures. However, for the room-temperature specimens, there is no width (W) change at low strains (e.g., RM1 - 3). In comparison, W increased in all low-temperature specimens after the impact. A larger dimension reduction in specimens' length (L) can also be seen in the low-temperature specimens, especially at low ε_{interr} (i.e., comparing between RM1 - 3 and CL1 - 4).

3.4. Damage characterisation

The internal micro-structural analysis indicates the voids occupy around 2‰ in the volume of all specimens, as shown in the column charts in Figs. 9a and 9b. Good consistency in void volume can be seen between the pre-scans and post-scans, especially for the specimens with slight and mild damage (e.g., RM1 - 3 and CL1 - 3). An internal damage

overview presented in Figs. 9c and 9d indicate higher ε_{interr} had led to larger damage in the specimens at both temperatures. More internal voids can be created during the process of loading, deforming and fracturing of RM4, RM5, CL4 and CL5.

However, the damage in low-temperature specimens appears to have an earlier initiation and more rapid evolution compared to room-temperature specimens, as observed in the previous work [26]. As shown in Figs. 9c and 9d, the damage observed in the tested specimens was categorised into six types based on its morphology and state - A. No damage; B. Transverse intra-ply cracking at surface layers; C. Transverse intra-ply cracking at multiple layers; D. Inter-ply delamination; E. Inclined intra-ply cracking; and F. Surface ply detached. The damage class - 'opened damage' in the present research specifically categorises the damage or crack with the width greater than 3 pixels, that is about 6.3 μm. Maximum specimen strain, ε_{interr} was taken from the DIC measurement and set as the reference for damage development analysis.

At room temperature, the specimens have no observable micro-scale damage with low ε_{interr} (RM1 and RM2), as shown in Fig. 9c. In the specimen with ε_{interr} = 4.56 % (RM3), the initiated intra-ply cracks can be seen at the surface layers propagated along the ply fibre direction and roughly aligned with the ply in-plane diagonal line (Fig. 8b) on both sides of the specimen. They slightly opened up near the impact face [26]. Apart from that, intra-ply cracks at their minimal size can also be found in the subsurface layers aligned with the surface layer intra-ply cracks in the through-width direction (highlighted by a pink arrow in Fig. 9c). The ε_{interr} of 8.25 % (RM4) produces intra-ply cracks not only in surface plies but also in subsurface plies (also see Fig. 10 (a - c)). Besides the transverse intra-ply cracks observed in RM3, inclined intra-ply cracks were also found (also see Fig. 11a). Delamination between the surface and second layers can be clearly seen. In addition, the through-length damage analysis of RM4 along the loading direction presented in Fig. 10c demonstrates the damage highly concentrates at the specimen's loading end. Similar damage distribution was also observed in existing literature [39, 40].

RM5 shows that a large volume of damage can be introduced after the specimens experienced a 13.45 % ε_{interr}. Intra-ply cracks and inter-ply delamination appeared throughout the specimen width (also see Fig. 10 (d - f)). Cracks are opened and inter-connected through inclined intra-ply cracks and ply delamination forming into a branch-shaped damage morphology and rooted at the lower part of the two middle plies (Ply 8 & 9). A semi-oval damage band (also see Fig. 11b) can be found on the impact face (Face B) and its two adjacent faces (Face A and D), as shown in Figs. 10e and 10f. The damage band on Face A was mainly formed by +45° intra-ply cracks and the associated delamination, whereas −45° cracks and the associated delamination compose the damage band on Face D. The semi-oval damage band on the impact face (Face B), however, is a combination of both +45° and −45° intra-ply cracks. The 3D bulk region encompassed by the damage bands on Face A and B are prominently more intact compared to the damage band regions. The through-length damage distribution shown in Fig. 10f indicates the damage is denser near the impact face of the specimen. However, its distribution along the specimen length is much more uniform compared to RM4.

Specimens at low temperatures started to have transverse intra-ply cracks at low strain levels (Fig. 9d). Transverse intra-ply cracks can already be found in surface and subsurface plies in CL1 (ε_{interr} of 2.55 %). No new damage categories were introduced in CL2 (ε_{interr} = 2.88 %), but the surface ply crack had started to open up. The initiated intra-ply cracks in CL1 and CL2 also propagated along the ply fibre direction and is approximately aligned with the ply in-plane diagonal lines as the room temperature specimens (highlighted by pink arrows in Fig. 9d). At ε_{interr} = 3.60 % (CL3), mild ply delamination occurred between the surface and the second plies. No obvious opened damage can be found in the rest of the regions in the specimen. On top of CL3, CL4 also has subsurface ply delamination between Ply 7 and 8. The transverse intra-ply crack that connects to the delamination opened up slightly near the impact face.

Compared to RM4 (ε_{interr} = 8.25 %), a strain of 8.91 % for low-temperature specimen (CL5) had resulted in larger damage as surface ply detachment on both sides of the laminates (also see Fig. 10 (g - i) and Fig. 11a). However, ply delamination can only be found between Ply 1 & 2, 2 & 3, 7 & 8 and is symmetric about the symmetry plane (also see Fig. 10h). Despite the ply detachment, the intra-ply cracks in CL5 are mainly in the transverse direction, different from the specimens with similar ε_{interr} but at room temperature (RM4). The damage distribution of CL5 along the loading direction (Fig. 10f) also indicates a high damage concentration near the impact face. The damage has a higher uniformity than that in RM4, but it is less uniform compared to RM5.

Fig. 12 presents the volume fraction of opened damage in the tested specimens. It can be seen that the opened damage increases with the increase of ε_{interr} for the specimens at both temperatures. Specimens at low temperatures with similar ε_{interr} as the room temperature specimens have substantially larger opened damage. Considering the detached volume, there is a 6.52 % damage fraction in CL5, which is even higher than the room-temperature specimens with much larger ε_{interr} (e.g., RM5).

4. Discussion

4.1. Damage development with mechanical response

Although the stress responses of the specimens between quasi-static loading (baseline), room- and low-temperature HSR loading are evidently different (Fig. 5), their apparent-yield strain (the sudden change in gradient, please see Fig. 5) all lie in the range from 3 to 4 %, indicating a low sensitivity of apparent-yield strain to the changes of temperature

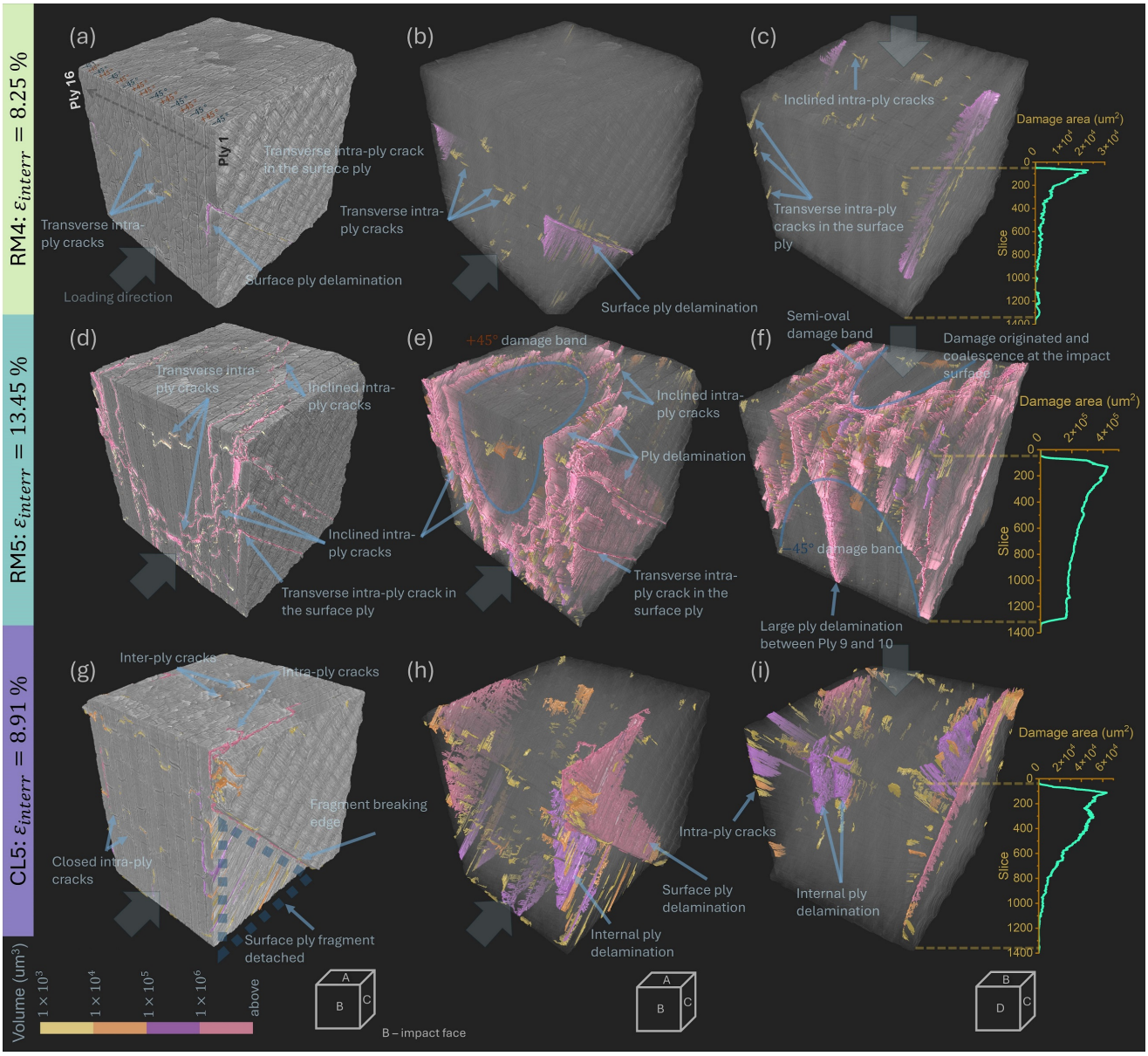


Figure 10: Tomographic reconstructions of opened damage in tested specimens. Specimen RM4: (a) damage with solid specimen body; (b) and (c) damage with transparent specimen body. Specimen RM5: (d) damage with solid specimen body; (e) and (f) damage with transparent specimen body. Specimen CL5: (g) damage with solid specimen; (h) and (i) damage with transparent specimen body. Damage is colour-coded based on size, and the colour map is presented in the bottom-left corner. The observation directions are noted at the bottom of each figure column. The damage distributions along the loading direction are plotted next to the 3D volume reconstruction in (c), (f) and (I).

and strain-rate within the tested ranges, as observed in the previous research [41].

Before the apparent-yield points, no micro-scale damage can be detected in RM1 and RM2 (Fig. 9c), implying that the specimens remain micro-structurally intact at room temperature. However, the specimen dimensions (mainly in L and H) changed permanently after the impact (Fig. 8c). That suggests the permanent deformation of the matrix, facilitated primarily through polymer chain rearrangement, has taken place in response to the intra-ply shear along the ±45° fibre directions. No ply delamination can be observed in RM1, RM2 and RM3 (Fig. 9c), corresponding to no permanent dimension expansion in their W direction (Fig. 8c). That is to say, before the apparent-yield point of the specimen, there is permanent deformation in L and H but not in W nor ply delamination in room-temperature specimens. At around ε_{interr} = 8.25 %, the specimens are still in a quasi-flowing state with negligible load-bearing capacity loss as reflected in Figs. 5a and 7a. High structural integrity, i.e. lower level of damage compared to low-temperature specimens, can be seen in specimen RM4. With the appearance of large and widespread opened damage at around ε_{interr} = 13.45 % (e.g.,

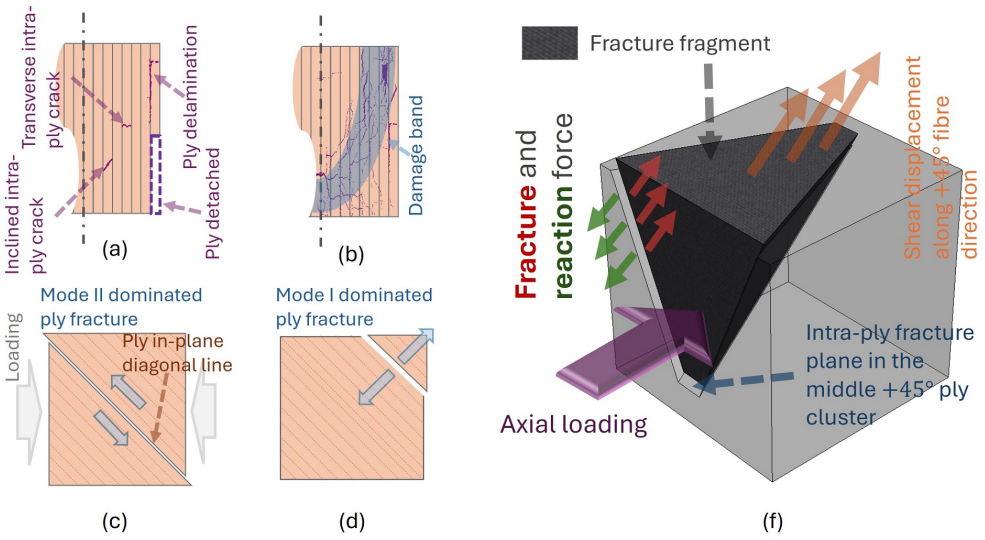


Figure 11: Observed damage features in sketches. (a) Different types of damage and (b) damage band observing from in-plane load direction. (c) Mode-II-dominated fracture caused directly by the in-plane compression, (d) Mode-I-dominated fracture caused by inter-ply shear and (e) hypothesis of the generation of V-shaped or semi-oval-shaped fractures: the specimens under axial impact causing a chunk of fragment displacing along the middle ply fracture.

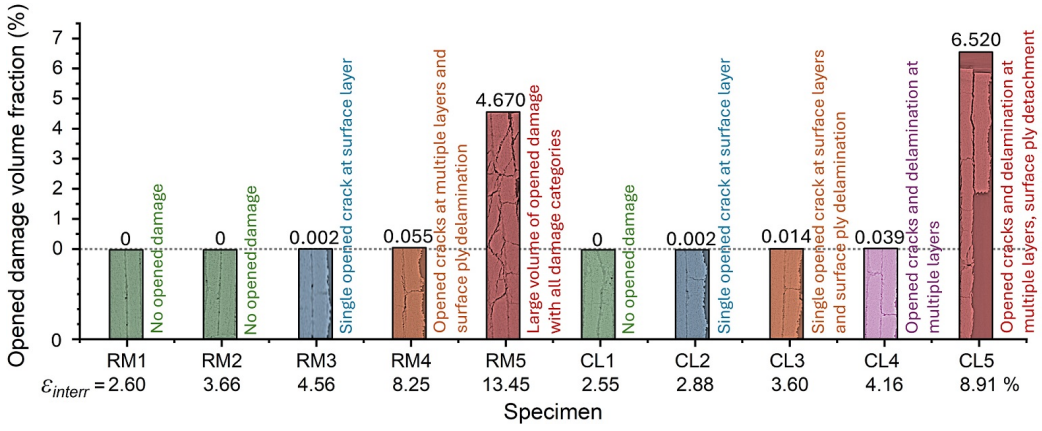


Figure 12: Opened damage development with the specimen strain increase and the description of key damage features. The damage volume fraction for specimen CL5 includes the detached volume. At similar strain levels, the specimens at low temperatures have significantly more opened damage than their room-temperature counterparts.

RM5), an evident stress drop can be found compared to the stress in the plateauing region (Fig. 7a).

In spite of the similar apparent-yield strain, at small strains the low-temperature specimens (CL1, CL2 and CL3) have already undergone permanent dimension change in all directions, including W due to inter-ply cracking (Fig. 8d and 9d). Given that the matrix dominates the W-direction deformation, the threshold for permanent deformation of the epoxy matrix might be lower at low temperatures [42]. The W-direction deformation was still within the fracture limit in CL1 and CL2. Delamination can only be observed at ε_{interr} = 3.60 % (CL3 in Fig. 9d), demonstrating that ply delamination can be generated around the apparent-yield point for the specimens at low temperatures, possibly due to the embrittlement of the epoxy matrix [43]. Similarly, the transverse intra-ply cracks initiated earlier than those in the room-temperature specimens. Distinct coefficients of thermal expansion between the carbon fibres and matrix [44] can introduce thermal stresses at the fibre/matrix interface after the cooling process. In addition to the matrix embrittlement, these pre-existing stresses will further contribute to the generation of the micro-scale cracks at the fibre/matrix interfaces upon loading. After the apparent-yield point and the occurrence of ply delamination, a pronounced decrease in specimen load-bearing capacity occurred (Fig. 5b). The level of delamination develops with the permanent dimension increase in W-direction (e.g., CL3 - CL5). At about

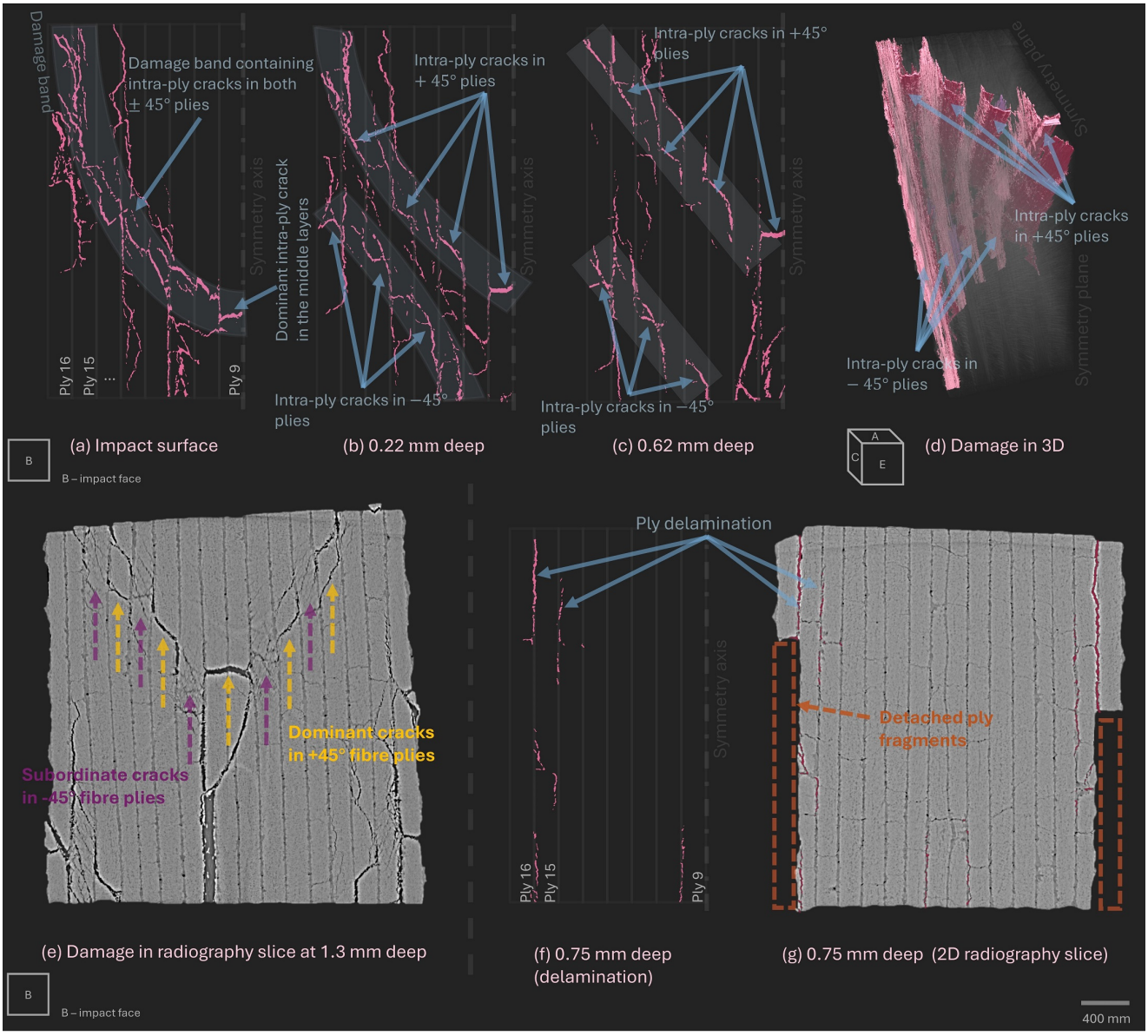


Figure 13: Opened damage in RM5 and CL5. For RM5: opened damage (a) at 0 mm, (b) 0.22 mm and (c) 0.62 mm deep from the impact surface of the specimen, (d) in 3D view and (e) shown in radiography slice at 1.3 mm deep. Damage developed along their ply fibre directions, causing damage in +45° plies propagated and drifted away from the damage in and −45° plies. For CL5: delamination at 0.75 mm deep from the impact surface: (f) damage segmented and (g) damage in radiography slice. Ply delamination is seen between Ply 1 & 2, 2 & 3, 7 & 8 and is symmetric about the middle plane. Face E is the face opposite to the impact face (Face B).

$\varepsilon_{interr} = 8.91\,\%$ (e.g., CL5), approximately 20 % of the specimen's load-bearing capacity had been lost (Fig. 5b). This is notable considering that no obvious decrease in load-bearing capacity can be seen in the room-temperature specimens at a similar strain level (e.g., RM4). This sudden loss in load-bearing capacity is, in essence, the mechanical reflection of the more rapid damage development at low temperatures, which in these specimens appears to be facilitated through ply delamination.

4.2. Damage initiation mechanisms

The damage morphology analysis referring to the strain levels demonstrates that the damage initiation mechanism is similar between room- and low-temperature specimens. It is in the sequence of micro-scale intra-ply cracks in both surface and subsurface plies, intra-ply cracks opening up in surface plies, surface ply delamination, intra-ply cracks opening up in middle plies, and middle ply delamination (Fig. 9c and 9d). Surface ply cracks tend to open up earlier since the surface plies (with fibres in −45°) have only one

side attached to the specimens and have no lateral and shear restraints on the surface sides.

At the damage initiation stage, the micro intra-ply cracks of the specimens at both temperatures are normally generated and propagate roughly along the ply in-plane diagonal line in the fibre direction (−45°). That indicates the intra-ply crack at this stage is mainly formed by ply mode II fracture where the intra-ply shear is produced by the ply fragments on opposing sides of the in-plane diagonal line displacing in opposite directions (Fig. 11c). At higher strains (e.g., RM4 and CL4), the existence of intra-ply cracks away from the ply in-plane diagonal line implies that those cracks might be produced by a mode-I/II-combined fracture (Fig. 11d). The source of this mode-I tensile stress can be the inter-ply shear in different directions caused by the deformation of neighbouring plies with different fibre directions and the volume expansion of specimens in the H-direction under L-direction compression.

The locations where opened damage appears after the surface layers for the specimens at both temperatures were found to be the cluster of two +45° plies in the middle on both sides of the symmetry plane (e.g., Fig. 9d - CL4). A Mode-II-dominated intra-ply crack was formed near the ply in-plane diagonal line (Fig. 13a) because of the *in-situ* shear strength reduction effect of clustered plies [45, 46].

4.3. Difference in damage propagation

Different damage mechanisms were noticed between room- and low-temperature specimens after the opened damage occurred in the middle +45° ply cluster. With compression progression in room-temperature specimens, the fracture fragment of the middle +45° ply cluster displaces further along the +45° intra-ply fracture plane (Fig. 11f). It stretches the neighbouring plies in the +45° fibre direction, posing mode-II shear stress to −45° plies and +45° plies both in the +45° fibre direction. That causes stress concentration along a semi-oval path surrounding the centre of mass of the fracture fragment and forms the damage band on the impact surface of RM5 (Figs. 10 (d - f) and Fig. 11f). However, this complex damage mechanic is a deduction from the damage morphology, future investigations are needed to verify this hypothesis.

Under HSR impact, the specimens do not deform uniformly along their length at the micro-scale level. High localised deformation and fracture occurred at the specimens' loading end prior to the rest of the region located deeper in the specimens' length according to the through-length damage distribution analysis in Fig. 10. The dominant open cracks in both +45 and −45° plies originate at the loading ends of the specimens, coalescing and aligning within a damage band (Fig. 13a). As the dominant open cracks propagate through specimen length, they grow along the ply fibre directions. Hence, the +45 and −45° ply cracks drift apart from each other, as shown in Figs. 13 (b - d). In a ply that is between two plies which have the same fibre direction (e.g., a −45° ply between two +45° plies), Mode-II-dominant cracks along the +45° fibre direction (sometimes small and discontinuous) formed and bridge the dominant cracks in the adjacent two plies (e.g., the two +45° plies), as shown in Fig. 13e. This damage propagation pattern produces the branch-shaped damage, as shown in Fig. 13d.

In contrast, specimens at low temperatures have different but simpler damage mechanisms at the later stages of loading. The observed damage morphology in low-temperature specimens implies that the epoxy matrix is stiffer and more brittle at low temperatures because of the low molecular kinetic energy. The testing temperature of −50° C is potentially below or near the beta-relaxation temperature (T_β) of the epoxy matrix [47]. The highly restricted molecular chain movement, low internal (inter- and intra-molecular) energy absorption and poor damping properties allow the impact energy to be effectively transmitted and accumulated at the weak points in the structure (that is, inter-ply resin-rich regions in this case), causing rapid fractures [48, 49]. This is also indicated by the early specimen volume expansion in the W-direction before the apparent-yield at low temperatures. Inter-ply weak points (i.e., the stress concentration regions) shift from the surface towards the middle layers with the continuous detachment of the outermost plies during loading, forming the damage morphology observed in Figs. 13f and 13g.

5. Conclusions

The micro-scale damage mechanisms of AP CFRP laminates under high strain-rate compressive loading were investigated by combining the use of SHPB loading platform, strain and momentum interruption techniques, high-speed visible light imaging, DIC, strain gauge measurement, synchrotron-based phase-contrast X-ray μ-CT, deep-learning-aided image segmentation and visualisation. It was demonstrated that the specimen maximum strain was effectively controlled at target values. The micro-scale damage initiation and evolution of the specimens at room and low temperatures were characterised, and the associated damage mechanisms were discussed.

In general, damage in low-temperature specimens initiates earlier and progresses more rapidly. Despite the different mechanical responses at different strain rates and temperatures, the apparent-yield point of all specimens occurs in the range of 3 to 4 % strain. The epoxy matrix itself, on the other hand, showcases higher brittleness at low temperatures. Although all specimens undergo permanent deformation before reaching their bulk apparent-yield stress, only the low-temperature specimens revealed intra-ply cracks, possibly attributed to the low failure strain of the matrix and the pre-existing thermal stress at the fibre/matrix interfaces. However, the existence of micro-scale intra-ply cracks does not seem to significantly impair the mechanical strength of the specimens; the rapid strength drop of the specimens is mainly dominated by inter-ply delamination. Whereas the opened cracks and delamination of room-temperature specimens initiated only after the apparent-yield point, they can be observed around the apparent-yield point at low

temperatures. The opened damage for the specimens at both temperatures initiated and concentrated at the impact end of the specimens.

For specimens at both temperatures, micro-cracks caused by mode-II fracture initiated at the surface and subsurface plies, with those in the surface plies the first to develop into opened damage. As the overall strain increased, mode-I/II-combined fracture also emerged, led by the specimen volume expansion and the excessive shear strain normal to the fracture direction. While specimens at both temperatures exhibit similar damage mechanisms initially, they show distinct ones after the occurrence of the opened damage in the middle +45° ply clusters. As the volume of opened damage increased with the strain, damage in the room-temperature specimens propagated mainly within damage bands resulting from the matrix's higher compliance. The energy was primarily dissipated through matrix deformation and crack formation. This mechanism facilitated the long strength-holding period (stress plateau) after the apparent-yield. However, inter-ply delamination and the resulting ply detachment from the outer to middle plies caused by the stress accumulation at inter-ply resin-rich regions are found to be the energy dissipation mechanism of low-temperature specimens at the late loading stages. This glassy behaviour is on account of the matrix's high strength but low failure strain at low temperatures, creating a pronounced stress drop after the apparent-yield points.

The 3D characterisation of micro-scale damage in CFRP laminates detailed in this work provides unique experimental insights into temperature-dependent failure mechanisms under high-rate loading. The thermo-mechanical interpretations will help to validate and advance discrete damage models for improved design and safety assessment of composite laminates, and to enhance the mechanistic understanding of complex micro-scale damage initiation and progression under real-world conditions.

CRediT authorship contribution statement

Xiyao Sun: Conceptualisation, Data curation, Formal analysis, Investigation, Methodology, Software, Validation, Visualization, Writing - Original Draft. **Bratislav Lukić:** Data curation, Methodology, Resource, Software, Writing - Review & Editing. **Kai Liu:** Investigation, Methodology, Writing - Review. **David Sory:** Investigation, Methodology, Writing - Review. **Maria Lissner:** Writing - Review & Editing. **Justus Hoffmann:** Writing - Review & Editing. **David Chapman:** Conceptualisation, Methodology, Supervision, Writing - Review & Editing. **Nik Petrinic:** Funding acquisition, Methodology, Project administration, Resource. **Daniel Eakins:** Conceptualisation, Funding acquisition, Methodology, Project administration, Resource, Supervision, Writing - Review & Editing.

Acknowledgements

The authors express their thanks to Drs Yanhong Chen and Ziwen Xu for assistance with the experiments at the ESRF, and also to the technician team at Begbroke Science Park for the manufacture of all specimens and equipment. The ESRF, Grenoble, France is acknowledged for providing standard access beamtime MA-5715 and in-house beamtime IHLS-3562. Funding for this research was provided by Innovate UK grant 113232: FANDANGO (FAN Design And iNtegrity, GO). B.L. acknowledges funding from the EPSRC (EP/W003333/1). Rolls-Royce plc is gratefully acknowledged for their continued support of the University Technology Centre in Solid Mechanics at the University of Oxford. Lastly, the authors wish to express special thanks to the late Prof Nik Petrinic, whose knowledge, guidance and support were vital to this work, and to the understanding of composites more widely.

References

[1] T. W. Clyne, D. Hull, An introduction to composite materials, Cambridge, third edition. edition, 2019.

[2] P. E. Irving, C. Soutis, Polymer Composites in the Aerospace Industry, Elsevier Science & Technology, San Diego, 2019.

[3] K. Wang, B. Young, S. T. Smith, Mechanical properties of pultruded carbon fibre-reinforced polymer (CFRP) plates at elevated temperatures, Engineering Structures 33 (2011) 2154–2161.

[4] Q. Sun, G. Zhou, H. Guo, Z. Meng, Z. Chen, H. Liu, H. Kang, X. Su, Failure mechanisms of cross-ply carbon fiber reinforced polymer laminates under longitudinal compression with experimental and computational analyses, Composites Part B: Engineering 167 (2019) 147–160.

[5] K. Takahashi, R. Higashiyama, G. Xue, T. Nakamura, In situ analysis of three-dimensional microcrack propagation in cross-ply laminates using synchrotron radiation X-ray computed tomography, Composites Science and Technology 258 (2024).

[6] L. Jiang, H. Xiong, T. Zeng, J. Wang, S. Xiao, L. Yang, In-situ micro-CT damage analysis of carbon and carbon/glass hybrid laminates under tensile loading by image reconstruction and DVC technology, Composites Part A: Applied Science and Manufacturing 176 (2024).

[7] H. Zhang, L. Yang, S. Ren, K. Wang, J. Li, In-situ experimental characterization and numerical investigation of the crack initiation of SMC composite under uniaxial tension, Composites Part A: Applied Science and Manufacturing 188 (2025).

[8] M. Ploeckl, P. Kuhn, J. Grosser, M. Wolfahrt, H. Koerber, A dynamic test methodology for analyzing the strain-rate effect on the longitudinal compressive behavior of fiber-reinforced composites, Composite Structures 180 (2017) 429–438.

[9] J. Arbaoui, M. Tarfaoui, A. El Malki Alaoui, Mechanical behavior and damage kinetics of woven E-glass/vinylester laminate composites under high strain rate dynamic compressive loading: Experimental and numerical investigation, International Journal of Impact Engineering 87 (2016) 44–54.

[10] T. Watanabe, Y. Takeichi, Y. Niwa, M. Hojo, M. Kimura, Nanoscale in situ observations of crack initiation and propagation in carbon fiber/epoxy composites using synchrotron radiation X-ray computed tomography, Composites Science and Technology 197 (2020).

[11] Y. Wang, M. J. Emerson, K. Conradsen, A. B. Dahl, V. A. Dahl, E. Maire, P. J. Withers, Evolution of fibre deflection leading to kink-band formation in unidirectional glass fibre/epoxy composite under axial compression, Composites Science and Technology 213 (2021) 108929.

[12] M. V. Hosur, J. Alexander, U. K. Vaidya, S. Jeelani, High strain rate compression response of carbon/epoxy laminate composites, Composite Structures 52 (2001) 405–417.

[13] M. Seyednourani, S. Akgun, H. Ulus, M. Yildiz, H. S. Sas, Impact damage and low temperature effects on carbon fiber/epoxy joints: A comparative study of hybrid bolted/bonded and bolted configurations

with cross-ply and angle-ply laminates, Composites Part A: Applied Science and Manufacturing 190 (2025).
[14] R. M. Guedes, M. F. de Moura, F. J. Ferreira, Failure analysis of quasi-isotropic CFRP laminates under high strain rate compression loading, Composite Structures 84 (2008) 362–368.
[15] J. Xiao, Z. Wu, Z. Pan, W. Ouyang, L. Shi, Analysis of in-plane compression failure mechanism in carbon fi ber braided composite with different off-axial angles 56 (2022) 2029–2046.
[16] T. J. Katafiasz, E. S. Greenhalgh, G. Allegri, S. T. Pinho, P. Robinson, The influence of temperature and moisture on the mode I fracture toughness and associated fracture morphology of a highly toughened aerospace CFRP, Composites Part A: Applied Science and Manufacturing 142 (2021).
[17] J. Meng, Y. Wang, H. Yang, P. Wang, Q. Lei, H. Shi, H. Lei, D. Fang, Mechanical properties and internal microdefects evolution of carbon fiber reinforced polymer composites: Cryogenic temperature and thermocycling effects, Composites Science and Technology 191 (2020).
[18] M. S. Islam, L. F. Benninger, G. Pearce, C. H. Wang, Toughening carbon fibre composites at cryogenic temperatures using low-thermal expansion nanoparticles, Composites Part A: Applied Science and Manufacturing 150 (2021).
[19] J. Körbelin, C. Dreiner, B. Fiedler, Impact of temperature on LVI-damage and tensile and compressive residual strength of CFRP, Composites Part C: Open Access 3 (2020).
[20] J. Körbelin, N. Junge, B. Fiedler, Modelling of low-velocity impact and compression after impact of CFRP at elevated temperatures, Composites Part A: Applied Science and Manufacturing 147 (2021).
[21] S. Sánchez-Sáez, T. Gómez-Del Río, E. Barbero, R. Zaera, C. Navarro, Static behavior of CFRPs at low temperatures, Composites: Part B 33 (2002) 383–390.
[22] Y. Ou, D. Zhu, H. Zhang, Y. Yao, B. Mobasher, L. Huang, Mechanical properties and failure characteristics of CFRP under intermediate strain rates and varying temperatures, Composites Part B: Engineering 95 (2016) 123–136.
[23] Y. Li, J. Meng, G. Niu, H. Yang, P. Wang, H. Lei, D. Fang, Cryogenic damage mechanisms of CFRP laminates based on in-situ X-ray computed tomography characterization, Composites Science and Technology 247 (2024) 110413.
[24] S. Morkavuk, U. Köklü, M. Bağcı, L. Gemi, Cryogenic machining of carbon fiber reinforced plastic (CFRP) composites and the effects of cryogenic treatment on tensile properties: A comparative study, Composites Part B: Engineering 147 (2018) 1–11.
[25] K. H. Im, C. S. Cha, S. K. Kim, I. Y. Yang, Effects of temperature on impact damages in CFRP composite laminates, Composites Part B:Engineering 32 (2001) 669–682.
[26] X. Sun, D. Sory, K. Liu, B. Lukić, D. Simonian, K. L. Wong, A. Rack, D. Chapman, N. Petrinic, D. Eakins, Effect of temperature on high strain-rate damage evolving in CFRP studied by synchrotron-based MHz X-ray phase contrast imaging, Composites Part B: Engineering 279 (2024).
[27] Y. Nie, N. D. Parab, J.-m. Chu, G. Kim, T. Sun, K. Fezzaa, R. Sterkenburg, W. W. Chen, Dynamic crack propagation from a circular defect in a unidirectional carbon fiber reinforced plastic composite, Journal of Composite Materials 52 (2018) 3539–3547.
[28] N. Pournoori, G. Corrêa Soares, B. Lukić, M. Isakov, M. C. L. Belone, M. Hokka, M. Kanerva, In situ damage characterization of CFRP under compression using high-speed optical, infrared and synchrotron X-ray phase-contrast imaging, Composites Part A: Applied Science and Manufacturing 175 (2023).
[29] P. Song, D. J. Chapman, A. M. Graham, B. Lukić, A. Rack, C. R. Siviour, Thermomechanical characterisation of a thermoplastic polymer and its short glass fibre reinforced composite: Influence of fibre, fibre orientation, strain rates and temperatures, Composites Part A: Applied Science and Manufacturing 180 (2024).
[30] J. M. Rodríguez-Sereno, J. Pernas-Sánchez, J. A. Artero-Guerrero, A. Rack, A. Vaz-Romero, J. López-Puente, D. Varas, F. Naya, A. Cohen, B. Lukić, Experimental compressive damage analysis on holed laminates under dynamic loadings using in-situ MHz synchrotron X-ray phase contrast imaging, Composite Structures 359 (2025).
[31] ASTM, Standard Test Method for In-Plane Shear Response of Polymer Matrix Composite Materials by Tensile Test of a 645° Laminate 1, Technical Report, American Society for Testing and Materials, 2018.
[32] G. Gray, Classic Split-Hopkinson Pressure Bar Testing, ASM Handbook 8 (2000).
[33] T. H. Le, P. J. Dumont, L. Orgéas, D. Favier, L. Salvo, E. Boller, X-ray phase contrast microtomography for the analysis of the fibrous microstructure of SMC composites, Composites Part A: Applied Science and Manufacturing 39 (2008) 91–103.
[34] D. Paganin, S. C. Mayo, T. E. Gureyev, P. R. Miller, S. W. Wilkins, Simultaneous phase and amplitude extraction from a single defocused image of a homogeneous object, Journal of Microscopy 206 (2002) 33–40.
[35] R. Kikinis, S. D. Pieper, K. G. Vosburgh, 3D Slicer: A Platform for Subject-Specific Image Analysis, Visualization, and Clinical Support, in: Intraoperative Imaging and Image-Guided Therapy, Springer New York, New York, NY, 2014, pp. 277–289.
[36] E. D'Imprima, M. Garcia Montero, S. Gawrzak, P. Ronchi, I. Zagoriy, Y. Schwab, M. Jechlinger, J. Mahamid, Light and electron microscopy continuum-resolution imaging of 3D cell cultures, Developmental Cell 58 (2023) 616–632.
[37] J. Fuller, M. R. Wisnom, Pseudo-ductility and damage suppression in thin ply CFRP angle-ply, Composites: Part A (2015) 64–71.
[38] J. E. Little, X. Yuan, M. I. Jones, Characterisation of voids in fibre reinforced composite materials, NDT and E International 46 (2012) 122–127.
[39] Z. Song, Z. Wang, H. Ma, H. Xuan, Mechanical behavior and failure mode of woven carbon/epoxy laminate composites under dynamic compressive loading, Composites Part B: Engineering 60 (2014) 531–536.
[40] J. Zhao, L. Guo, L. Zhang, X. Wang, Y. Tang, Z. Li, Experimental investigations on the in-plane dynamic compressive behavior and upper limit of constant strain rate for 2D twill weave carbon fiber reinforced composite, Composites Part B: Engineering 220 (2021).
[41] J. Gu, Y. Bai, Z. Zhao, C. Zhang, Temperature and strain rate sensitivity of modulus and yield strength of epoxy resin under compressive loads, Polymer 295 (2024).
[42] H. Chen, P. Song, T. Commins, A. Graham, A. R. Trivedi, C. R. Siviour, Characterization and modelling of bisphenol-a type epoxy polymer over a wide range of rates and temperatures, Polymer 249 (2022).
[43] W. Araki, D. Asahi, T. Adachi, A. Yamaji, Time-temperature dependency of mode II fracture toughness for bisphenol a type epoxy resin, Journal of Applied Polymer Science 96 (2005) 51–55.
[44] R. Ruiz-Iglesias, R. Cappello, O. T. Thomsen, J. M. Dulieu-Barton, Estimating the coefficients of thermal expansion of carbon fibre composite materials using infrared thermography, Composites Part A: Applied Science and Manufacturing 198 (2025).
[45] G. J. Dvorak, N. Laws, Analysis of Progressive Matrix Cracking In Composite Laminates II. First Ply Failure, Technical Report, ????
[46] P. P. Camanho, C. G. Dávila, S. T. Pinho, L. Iannucci, P. Robinson, Prediction of in situ strengths and matrix cracking in composites under transverse tension and in-plane shear, Composites Part A: Applied Science and Manufacturing 37 (2006) 165–176.
[47] L. Q. Reyes, S. R. Swan, H. Gan, S. M. Seraji, J. Zhang, R. J. Varley, The role of β relaxations in determining the compressive properties of an epoxy amine network modified with POSS and mono-functional epoxy resins, Polymer Testing 93 (2021).
[48] N. Shito, M. Sato, Electrical and mechanical properties of anhydride-cured epoxy resins, Journal of Polymer Science Part C: Polymer Symposia 16 (1967) 1069–1078.
[49] O. Vryonis, A. S. Vaughan, T. Andritsch, P. H. Morshuis, A. Claverie, On Molecular Dynamics and Charge Transport in a Flexible Epoxy Resin Network, Materials 15 (2022).